

A unified soil reaction model for laterally loaded monopiles in soft and stiff clays

Xiuyang Zhang^{a,b}, Degao Zou^{a,b,*}, Jingmao Liu^{a,b,*}, Kai Chen^{a,b}, Fanwei Ning^{a,b}, Tianju Wang^{a,b}

^a The State Key Laboratory of Coastal and Offshore Engineering, Dalian University of Technology, Dalian, Liaoning 116024, China

^b Department of Hydraulic Engineering, Dalian University of Technology, Dalian, Liaoning 116024, China

ARTICLE INFO

Keywords:

Monopiles

Clay

Soil reaction model

Base shear force and base moment

Pile side shear stress

ABSTRACT

To develop a unified soil reaction model suitable for laterally loaded monopiles in soft and stiff clays, this paper employs an experimentally validated numerical method to analyze the influence of diameter, embedded length (L), and clay types (soft or stiff) on the soil reaction model, proposing a unified model based on hyperbolic soil reaction curve. This model fully considers the contributions of distributed lateral load, base moment, base shear force, and distributed moment to the lateral resistance. The results of the analysis indicate that the ultimate normalized lateral soil resistance (\bar{p}_u) of soft and stiff clays in the wedge flow zone increases with depth, reaching a peak in the full flow zone with the peak points located around $0.5L$. The maximum of \bar{p}_u between soft and stiff clays is positively correlated with the ratio of effective vertical stress to undrained shear strength (σ'_v/s_u) at the current depth. The ultimate base shear force and base moment for monopiles in soft and stiff clays can also be represented by σ'_v/s_u at the base. Through rigorous validation with centrifuge and field tests, the unified soil reaction model proposed in this paper can accurately predict the response of monopiles in soft and stiff clays.

1. Introduction

Monopile foundations have gradually become the mainstream choice in the offshore wind industry because of the simplicity of design and construction. Throughout the lifecycle of offshore wind turbines, monopile foundations must withstand horizontal force and overturning moment generated by environmental loads such as wind, waves, and currents. Thus, accurately evaluating the behaviour of monopile under lateral loading is crucial for ensuring the overall stability and safe operation of the wind turbine.

The p - y method, deduced from the Winkler foundation beam model, is an extensively computational method for analyzing the lateral load response of monopiles. Currently, the p - y curves proposed in the API (2014) guideline were initially derived by Matlock (1970) based on field tests of small-diameter flexible piles with a diameter $D = 0.324$ m and an aspect ratio $L/D = 39$ in the offshore oil and gas industry. In recent years, with the increase in installed capacity of offshore wind turbines, the monopile diameters used in the project has reached 10 m and may even reach 12 m in the future, while the L/D ratio has decreased to between 2 and 8 (Chen et al., 2023), which significantly differs from the

deformation characteristics of small-diameter flexible piles. If the p - y curves based on flexible piles are used to analyze rigid piles with small length-diameter ratios, it will result in an underestimation of the lateral resistance of monopiles. (Wang et al., 2020; Lai et al., 2021). This is because the failure mode of monopiles has shifted from the bending failure mode of flexible piles to the rotational failure mode of rigid piles (Hong et al., 2017). Additionally, the DNV (2016) standard suggests that the application of the p - y method for the analysis of monopile lateral load characteristics must be validated by the finite element method, which further increases the workload of monopile design.

To improve the accuracy of the p - y method when analyzing monopiles under lateral loads, numerous improved soil reaction models have been proposed (Jeanjean, 2009; Yu et al., 2017a; Zhang and Andersen, 2019; Fu et al., 2020; Lai et al., 2021; Jiao et al., 2024). Most of these models are modifications of existing p - y curves according to experimental results or numerical simulations (Yu et al., 2017b; Li et al., 2018; Truong and Lehane, 2018; Li et al., 2020; Zhu et al., 2022). Truong and Lehane (2018) found through a series of centrifuge experiments that the net ultimate pressures were significantly correlated with the normalized embedment depth of monopiles and the undrained shear

* Corresponding authors at: The State Key Laboratory of Coastal and Offshore Engineering, Dalian University of Technology, Dalian, Liaoning 116024, China.
E-mail addresses: zoudegao@dlut.edu.cn (D. Zou), liujm@dlut.edu.cn (J. Liu).

strength, proposing a p - y curve suitable for soft clay foundations that accounts for the shape of the monopile. [Zhu et al. \(2022\)](#) explained the mechanism of pile-soil interaction and suggested an accurate analytical p - y curve model incorporating the small-strain stress-strain relation. There is also a category of models based on the deformation mechanism of monopiles (as illustrated in [Fig. 1](#)), incorporating multi-spring soil reaction models that account for additional pile side shear stress, base shear force, and base moment, as shown in [Table 1](#). [Jiao et al. \(2024\)](#) established the analytical expressions for three-spring model and proposed a calculation method that can accurately predict the lateral bearing capacity of the monopile. However, most of the aforementioned numerical models are based on research results obtained from single-type clay (soft or stiff) foundations. Since the small-strain shear modulus and undrained shear strength of soft clay are lower than those of stiff clay, the soil reaction model proposed solely based on numerical analysis results from soft clay is not suitable for the lateral loading analysis of monopiles in stiff clay, and vice versa. Therefore, there is a lack of systematic research on soil reaction models that can be applied to both soft and stiff clay foundations.

To enhance the applicability of soil reaction models to different site conditions, [Zhang and Andersen \(2017\)](#) and [Lai et al. \(2021\)](#) introduced an analytical method to precisely obtain soil reaction curves by scaling the soil stress-strain curves. [Souri et al. \(2023\)](#) developed a unified p - y curve for undrained clay sites by establishing relationships between undrained shear strength, effective unit weight, embedment depth, pile diameter, and the ultimate soil resistance. The PISA model ([Byrne et al., 2020a](#)) is primarily suitable for analyzing monopiles under lateral loading in stiff clay, but their suitability for soft clay foundations has not been sufficiently validated. Furthermore, the conic function soil reaction curves employed in the PISA project complicate the calibration process for specific sites. Therefore, developing a unified four-spring soil reaction model that can be applied to both soft and stiff clay foundations to address complex site conditions has become an urgent issue in large-diameter monopiles lateral load analysis.

In response to these challenges, this paper conducts finite element

analyses of monopiles in three clay foundations, utilizing calibrated real-site clay constitutive parameters and validated numerical methods. Through systematic analysis, this paper recommends relationships between undrained shear strength, effective vertical stress, embedment depth, and diameter with the ultimate soil resistance and proposes a four-spring soil reaction model based on hyperbolic curves. The proposed model can adequately take into account the influence of the rotational deformation mode of monopiles and is suitable for analyzing monopiles under lateral loading in soft and stiff clays. Through comparative analysis with the PISA model, the model proposed in this paper demonstrates its accuracy and applicability under various site conditions.

2. Numerical analysis method

2.1. Mesh and boundary conditions

Numerical analysis was performed using the geotechnical finite element software GEODYNA ([Gong et al., 2023](#); [Qu et al., 2021](#); [Zhang et al., 2024](#); [Zou et al., 2013](#); [Zou et al., 2022a](#)). To enhance computational efficiency, a refined three-dimensional cross-scale mesh was generated through the application of symmetry and octree mesh discretization techniques, as illustrated in [Fig. 2](#). The high-precision nonlinear scaled boundary finite element was used to simulate the polyhedron elements generated during discretization ([Chen et al., 2017](#)), while the remaining elements were simulated using isoparametric element. The mesh sensitivity analysis reveals that after doubling the grid density, the load-displacement response of the model changes by less than 2 %, which means the computational accuracy requirements are fulfilled ([Wang et al., 2022](#)). The mesh eventually used consists of 125,643 elements, as shown in [Fig. 2](#). Subsequent numerical analyses were conducted by coupling the finite element method with the scaled boundary finite element method. In order to reduce the influence of the model boundary, the length from the monopile shaft to the lateral boundary was set at $10D$, and the spacing between the pile base and the

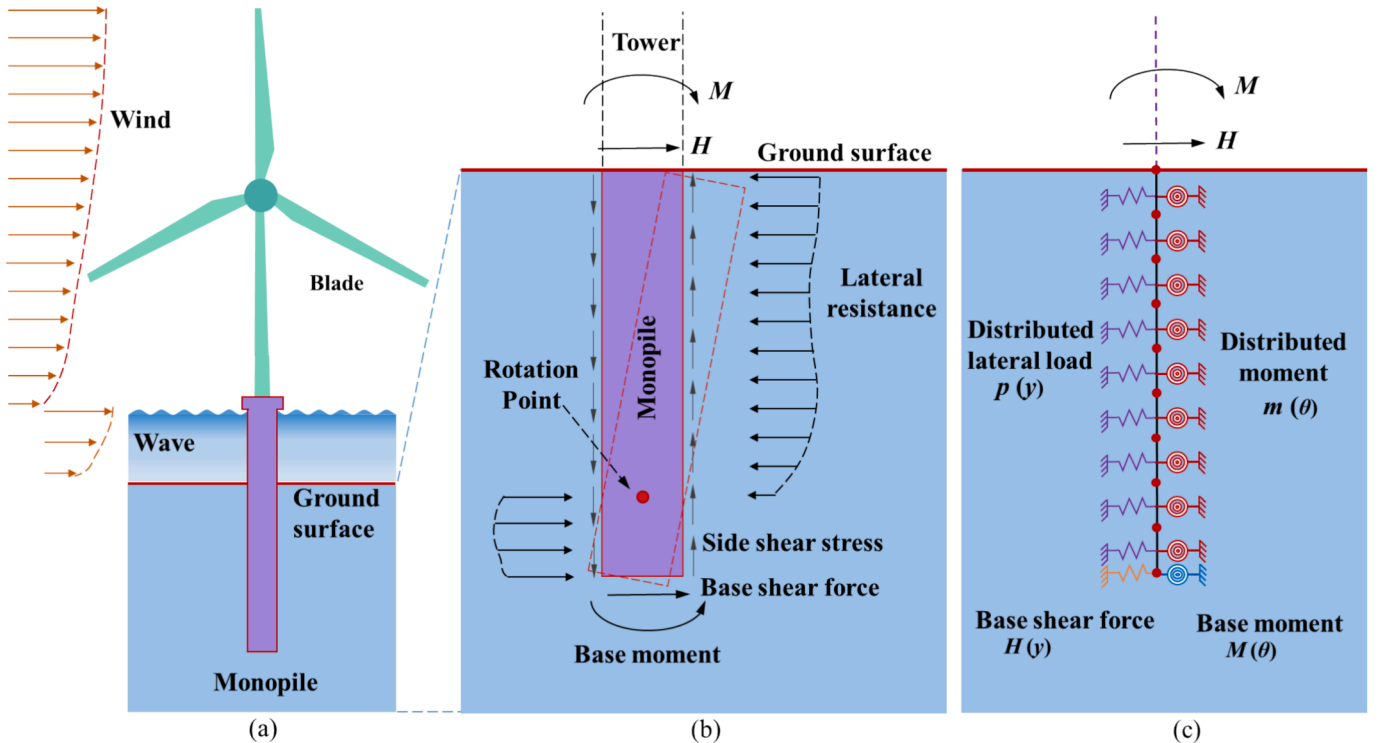


Fig. 1. Typical monopile foundation ([Zhang et al., 2024](#)) (a) Wind turbine and monopile under lateral loads. (b) Representation of soil reaction forces (c) Four types of soil reaction spring.

Table 1
Existing soil reaction models.

References	Clay type	p - y springs	m - θ springs	H - y spring	M - θ spring	Concentrated rotational spring
Zhang and Andersen (2017)	Unified clay	✓	—	—	—	—
Li et al. (2020)	Unified clay	✓	—	—	—	—
Zhu et al. (2022)	Soft clay	✓	—	—	—	—
Souri et al. (2023)	Unified clay	✓	—	—	—	—
Zhang and Andersen (2019)	Unified clay	✓	—	✓	—	—
Fu et al. (2020)	Soft clay	✓	✓	✓	—	—
Byrne et al. (2020a)	Stiff clay	✓	✓	✓	✓	—
Cao et al. (2021)	Soft clay	✓	—	✓	✓	—
Wang et al. (2020)	Soft clay	✓	—	—	—	✓
Lai et al. (2021)	Unified clay	✓	—	—	—	✓
Shao et al. (2024)	Stiff clay	✓	✓	—	—	✓
Jiao et al. (2024)	Unified clay	✓	✓	—	—	✓

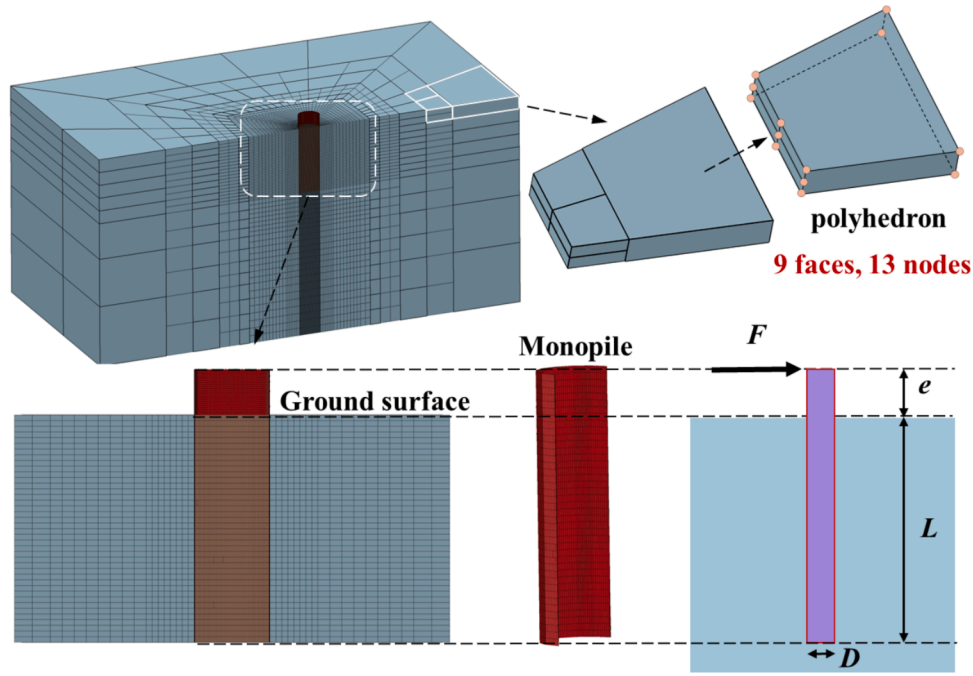


Fig. 2. 3D finite element mesh (Zhang et al., 2024).

bottom boundary was set at $5D$ (Zhang et al., 2024). The lateral surface and bottom of the computational model were constrained using lateral and pinned supports, respectively.

2.2. Constitutive model

The pile-soil interaction (PSI) of laterally loaded monopiles represents a complex three-dimensional problem, and the effective simulation of PSI depends heavily on the ability of the constitutive model to accurately reflect the highly nonlinear properties of clay. Considering these factors, the clay is modeled using the generalized plasticity constitutive model, which was initially proposed by Pastor and Zienkiewicz (Pastor et al., 1985; Pastor et al., 1990). The model has been successfully employed to reproduce the nonlinear behavior of clay for practical applications. Building on this foundation, Xu et al. (2012) integrated it into the geotechnical engineering software GEODYNA, and it has been successfully used to analyze static and dynamic geotechnical structures such as earth-rock dams (Qu et al., 2020; Gong et al., 2023) and offshore wind monopile foundations (Zhang et al., 2024).

The elastoplastic stiffness matrix \mathbf{D}^{ep} is expressed as:

$$\mathbf{D}^{ep} = \mathbf{D}^e - \frac{\mathbf{D}^e : \mathbf{n}_g : \mathbf{n}_g^T : \mathbf{D}^e}{H + \mathbf{n}_g^T : \mathbf{D}^e : \mathbf{n}_g} \quad (1)$$

where, \mathbf{D}^e is the elastic stiffness matrix, \mathbf{n}_g is the plastic flow direction vector, H is plastic modulus under loading and reloading.

\mathbf{n}_g can be obtained as follows:

$$\mathbf{n}_g = (n_{gv}, n_{gs})^T = \left(\frac{d_g}{\sqrt{1 + d_g^2}}, \frac{1}{\sqrt{1 + d_g^2}} \right)^T \quad (2)$$

where, d_g is the stress-dilatancy relationship.

Other constitutive parameters are not given in this paper, as detailed in Xu et al. (2012).

2.3. Undrained conditions

The effective stress analysis under undrained conditions is implemented by separately defining the effective elastoplastic matrix of the soil skeleton (\mathbf{D}^{ep}) and the pore water pressure matrix (\mathbf{D}^w), which are subsequently superimposed to form the total stress matrix (\mathbf{D}). The method was initially proposed by Naylor (1974), and Zou et al. (2022b) integrated it into GEODYNA, establishing a simplified and efficient fluid-solid coupling analysis method under undrained conditions.

The pore water pressure matrix \mathbf{D}^w can be expressed as:

$$D^w = \frac{K_w}{n} \begin{pmatrix} I & 0 \\ 0 & 0 \end{pmatrix} \quad (3)$$

where, K_w is the compressive modulus of water ($K_w = 2.08 \times 10^6$ kPa), n is the soil porosity, 0 is the 3×3 null matrix, and I is the 3×3 identity matrix.

The following formula can be used to determine the relationship between the increment of pore water pressure and strain:

$$dP_w = D^w : de \quad (4)$$

2.4. Pile-soil interaction

The pile-soil interface is simulated using zero-thickness Goodman interface elements (Goodman et al., 1968). The relationship between stress and displacement for the interface elements is determined by the following equation (Zou et al., 2013):

$$\begin{Bmatrix} \Delta F_{zx} \\ \Delta F_{zy} \\ \Delta F_{zz} \end{Bmatrix} = \begin{Bmatrix} k_{zx} & 0 & 0 \\ 0 & k_{zy} & 0 \\ 0 & 0 & k_{zz} \end{Bmatrix} \begin{Bmatrix} \Delta \delta_{zx} \\ \Delta \delta_{zy} \\ \Delta \delta_{zz} \end{Bmatrix} \quad (5)$$

where, ΔF_{zx} and ΔF_{zy} are the increments of shear stress, k_{zx} and k_{zy} are the shear stiffness, $\Delta \delta_{zx}$ and $\Delta \delta_{zy}$ is the increment of shear displacement in the shear direction. ΔF_{zz} is the normal stress, $\Delta \delta_{zz}$ and k_{zz} are the increments of normal displacement and normal stiffness, respectively.

A state-dependent perfect elastoplastic interface model (Zou et al., 2013) is employed to establish the contact characteristics of pile-soil interaction.

3. Validation of numerical simulation method

To demonstrate the fidelity of the numerical analysis method to simulate the laterally loaded response of monopiles in undrained clay foundations, both field tests on rigid piles in stiff clay and centrifuge tests on large-diameter monopiles in soft clay were selected. Additionally, parameter calibration of the Bangkok clay was carried out to provide conditions for subsequent studies on the unified soil reaction model.

3.1. Constitutive parameters

The parameter calibration process for Kaolin clay, Bangkok clay, and Cowden stiff clay is as follows: (1) determine the elastic parameters (coefficients and exponents of small-strain shear modulus and bulk modulus) and critical stress ratio based on literature data (Surarak et al., 2012; Likitlersuang et al., 2013; Zdravković et al., 2019; Byrne et al., 2020b; Duque et al., 2021; Duque et al., 2022); (2) calibrate the remaining constitutive parameters according to the stress-strain curves from triaxial tests. The final parameters are shown in Table 2, and the stress-strain relationship and pore water pressure-axial strain relationship from the undrained triaxial tests and calibrations are shown in Figs. 3–5. The effective unit weight (γ') and undrained shear strength (s_u) of Kaolin clay, Bangkok clay, and Cowden stiff clay are shown in Table 3.

Based on the finding by Zhang et al. (2024), the shear stiffness coefficient and exponent of the perfect elastoplastic interface have little influence on the laterally loaded behavior of monopiles. Thus, the parameters in this paper are consistent with their findings. To prevent

penetration of the interface, the compression stiffness coefficient k_2 is set at 1×10^7 kPa, and the strength of the interface is taken as 2/3 of the soil critical state friction angle. Table 4 shows the specific parameters.

3.2. Validation of centrifuge test and field test

The validation was conducted through the following tests. (1) A series of scaled monopile tests (Byrne et al., 2020b) were conducted in the Cowden stiff clay in the UK as part of the PISA project. The CM2 pile was selected for validation in this study. The pile dimensions are listed in Table 5, and the soil constitutive parameters are listed in Table 2. The load-displacement relationship curve, pile shaft displacement, and bending moment calculated in this study agree with the test results, as illustrated in Fig. 6 and Fig. 7. (2) Lai et al. (2020) investigated the lateral load response of monopiles in soft clay under lateral loading through a series of centrifuge tests. The monotonic tests were selected for validation in this study. As shown in Fig. 8, the load-displacement relationship curve obtained by the numerical simulation matches the test results, confirming that the method used in this study can be applicable to the analysis of laterally loaded characteristics of large-diameter monopiles.

4. Development of the united soil reaction models

4.1. Program for numerical parametric analysis

Table 6 presents the program for the parametric analysis of monopiles in this study. The monopile thickness is calculated based on the Eq. (6) (API, 2014), with an elastic modulus $E = 210$ GPa and a Poisson's ratio $\nu = 0.3$. The calculation range covers the diameters and embedment lengths currently and potentially planned for offshore wind farms, with aspect ratios ranging from 2.5 to 8.33. Following the research results of Wang et al. (2022), the load eccentricity has no significant influence on the soil reaction curve. Therefore, the load eccentricity in this paper is uniformly set at 100 m.

$$t = 0.006 + \frac{D}{100} \text{ (m)} \quad (6)$$

Based on the research basis of the PISA project (Byrne et al., 2020a), the vertical load carried by the monopile is usually only a small fraction of the vertical bearing capacity of the foundation. Therefore, consistent with the PISA project (Byrne et al., 2020a), this study is also based on the conventional design assumption for laterally loaded monopiles, namely that the lateral load-bearing capacity of monopiles supporting wind turbines is not influenced by the vertical loads (induced by the weight of the wind turbine and tower structure).

4.2. Quantifying the contribution of the soil reaction components

From the deformation mode of the monopile illustrated in Fig. 1 and referencing the findings of Hong et al. (2017), it is evident that the failure mechanisms of large-diameter monopiles primarily include wedge failure mechanism at the shallow zone, full flow mechanism below the wedge zone, and rotational failure mechanism at the base. Compared to small-diameter flexible piles (without rotational deformation), rotational deformation mode significantly enhances the base moment, base shear force, and pile side distributed moment in resisting lateral loads. To illustrate the impact of the soil reaction models on the

Table 2
Parameters of the constitutive model for clay.

	G_0	K_0	M_g	M_f	α_f	α_g	H_{u0}	H_{10}	m_v	m_l	m_s	β_0	β_1	γ_{dm}	r_d	γ_u	m_u
Kaolin clay	72	70	0.90	0.5	0.42	-0.4	100	100	0.65	0.5	0.65	10	0.02	15	10	3.5	0.6
Bangkok clay	260	346	1.07	0.85	0.55	-0.89	100	100	0.5	0.10	0.50	10	0.01	15	10	3.5	0.6
Cowden stiff clay	1478	2349	1.07	1.01	0.55	-0.96	2400	700	0.42	0.35	0.42	35	0.025	15	10	3.5	0.6

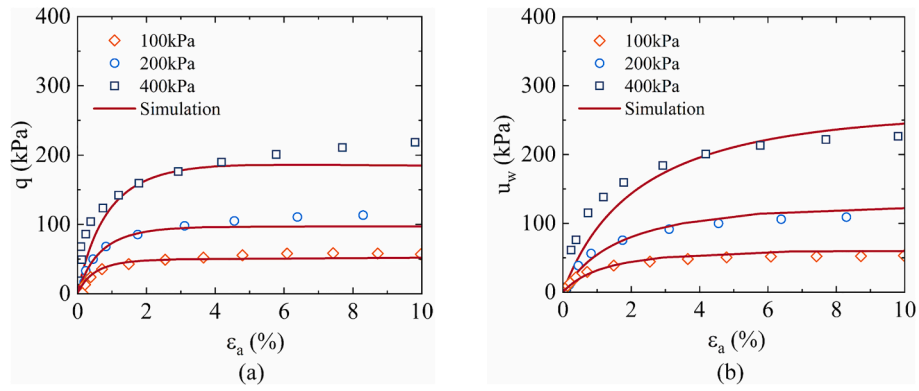


Fig. 3. Comparison between experimental data and simulation results for Kaolin clay (a) $\varepsilon_a - q$; (b) $\varepsilon_a - u_w$.

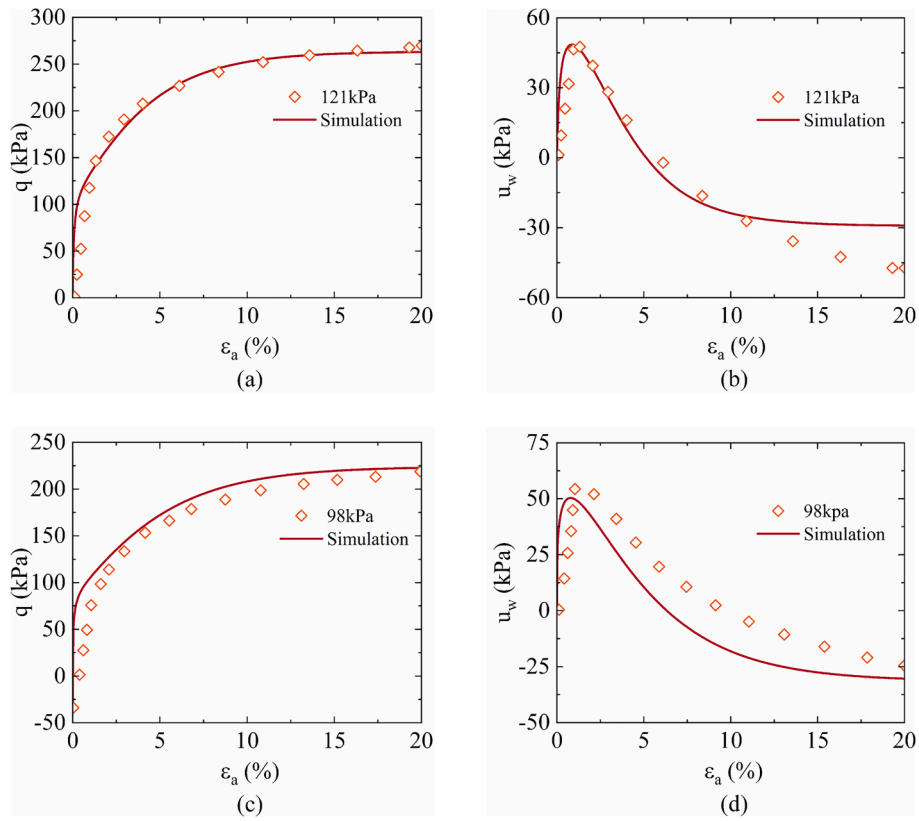


Fig. 4. Comparison between experimental data and simulation results for Cowden stiff clay (a) $\varepsilon_a - q$; (b) $\varepsilon_a - u_w$; (c) $\varepsilon_a - q$; (d) $\varepsilon_a - u_w$.

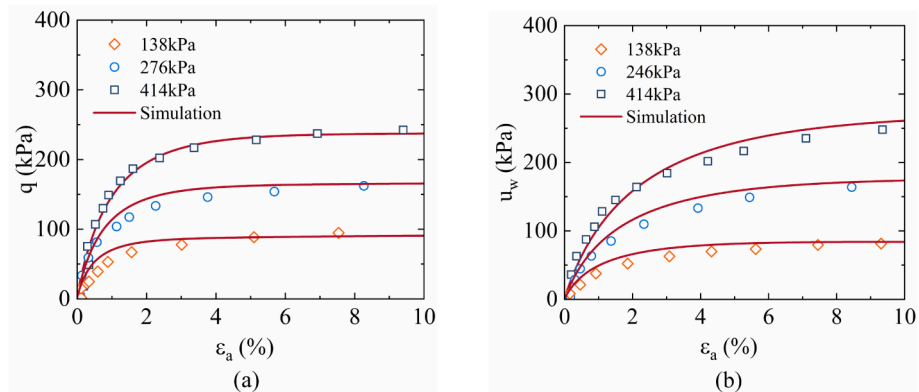


Fig. 5. Comparison between experimental data and simulation results for Bangkok clay (a) $\varepsilon_a - q$; (b) $\varepsilon_a - u_w$.

Table 3
Effective unit weight and undrained shear strength of clay.

	s_u (kPa)	γ' (kN/m ³)	References
Kaolin clay	1.65z	6.5	Duque et al. (2021); Duque et al. (2022)
Bangkok clay	3.3z	10	Surarak et al. (2012); Likitlersuang et al. (2013)
Cowden stiff clay	70 + 6.73z	11.37	Zdravković et al. (2019)

Table 4
Parameters of perfect elastoplastic interface.

k_1	k_2 (kPa/m)	n	φ
800	1×10^7	0.5	16

Table 5
Detailed dimensions of the monopiles used for validation.

	Embedded length D (m)	Diameter D (m)	L/D	Thickness t (m)	Load eccentricity (m)
PISA (Byrne et al., 2020b)	10.5	0.762	7.5	0.025	10
Lai et al. (2020)	60	4	5	0.08	8

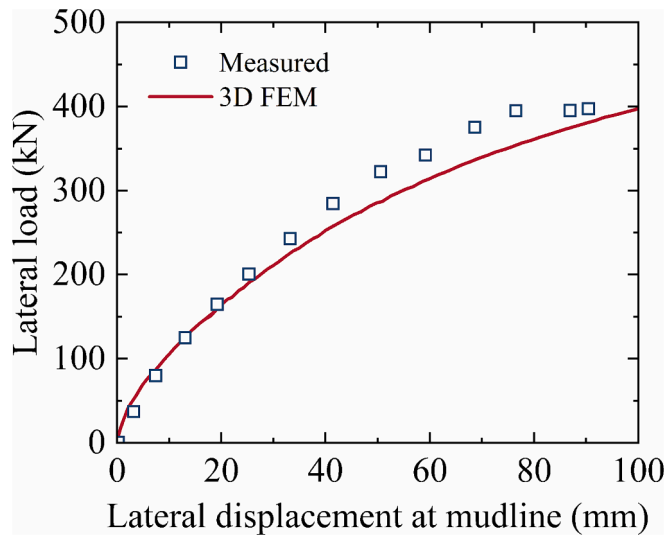


Fig. 6. Lateral displacement versus load relationship curve at mudline.

lateral responses of large-diameter monopiles, Fig. 9 compares the load–displacement relationship obtained using the extracted soil reaction curves from numerical simulations and the API method with the results of the finite element method. The lateral soil resistance p contributes the most to the ability of monopiles to resist horizontal deformation, while the roles of the other three types of resistance are also significant. The API practice significantly underestimates the ability of monopiles to resist horizontal deformation. The contributions of base moment base shear force and pile side shear stress to monopiles in Kaolin clay with different aspect ratios (L/D) were quantified based on numerical analysis results, as detailed in Fig. 10. Besides the distributed lateral load (p), the proportions of the distributed moment (m), pile base shear force (H), and base moment (M) all increase as the aspect ratio (L/D) decreases, reaching a maximum of 11 %, 8 %, and 7 %, respectively.

This is because as the length-to-diameter ratio decreases, the rotational deformation mode becomes more significant, causing monopiles to approach the failure mechanism of the rigid pile, resulting in increased pile base deformation. It is therefore essential to consider the four components of soil resistance in a comprehensive manner rather than just taking into account the contribution of the distributed lateral load p - y springs when designing and analyzing monopiles. This approach can reduce construction costs, increase economic efficiency, and more accurately calculate the laterally loaded response of monopiles.

4.3. Description of the soil reaction model

As shown in Fig. 11(a), the lateral soil resistance p of the laterally loaded monopile is composed of normal soil resistance along the pile perimeter and tangential shear stress. The ultimate lateral soil resistance exerted by the soil on the monopile can be expressed as:

$$p = Q + F \quad (7)$$

where, Q is the soil resistance generated by normal stress; F is the soil resistance generated by tangential shear stress. F and Q can be calculated using the following equations:

$$Q = \sum_{i=1}^n p_i \quad (8)$$

$$F = \sum_{i=1}^n \tau_i \sin \varphi \quad (9)$$

where, p_i represents the horizontal component of the normal stress acting on the pile element; τ_i denotes the horizontal component of the shear stress acting on the pile element; n represents the number of pile elements in the cross-section.

The distributed moment m in the cross-section of monopile is determined by integrating the pile side shear stress t_z , as follows:

$$m = \int_0^{2\pi} t_z D^2 \cos \varphi d\varphi \quad (10)$$

The vertical shear stress t_z and the variable θ are shown in Fig. 11(b).

The pile base shear force and base moment were determined by integrating the stress on the pile tip element and soil plug element. The relative displacement and cross-sectional rotations of the monopile are calculated by averaging the relative displacements and cross-sectional rotations of all pile elements at the corresponding depth.

In this paper, the variables of soil resistance and deformation for all soil reaction curves (distributed lateral load, distributed moment, base shear force, and base moment) are described in dimensionless form, as shown in Table 7. Additionally, the backbone curves of the soil reaction model include hyperbolic tangent function (Jeanjean, 2009; Cao et al., 2021; Zhu et al., 2022) and hyperbolic function (Zhou et al., 2020; Liu and Jiang, 2024; Zhang et al., 2024). This paper uses the hyperbolic function to describe all normalized soil reaction curves. Taking the normalized p - y curve as an example in Eq. (11), \bar{y} is the normalized lateral displacement, \bar{p}_u is the normalized ultimate soil resistance, and k_p is the initial stiffness.

$$\bar{p} = \frac{\bar{y}}{(1/k_p) + (\bar{y}/\bar{p}_u)} \quad (11)$$

Fig. 1(c) describes the one-dimensional finite element framework of the soil reaction model, in which the monopile is simulated using a two-node, five degree-of-freedom Timoshenko beam element (Byrne et al., 2020a), and the soil reaction springs acting on the monopile are modeled using the same interpolation functions as the monopile elements. The integration in the calculation process is carried out using Gaussian integration with four Gaussian points, and the nonlinear equations are solved using the Newton-Raphson method. Therefore, by

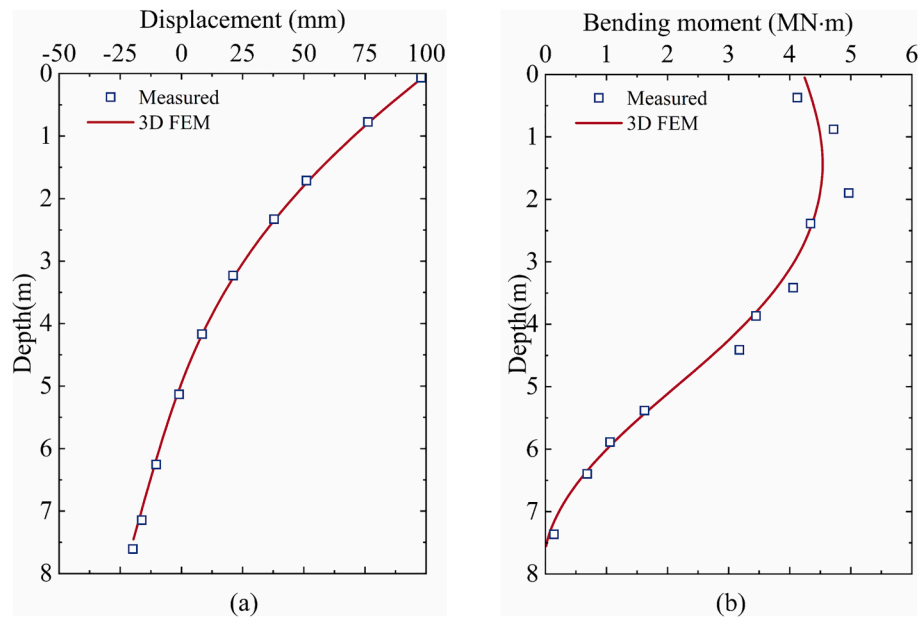


Fig. 7. Comparison of field test and numerical simulation of laterally loaded response of monopile. (a) Shaft displacement (b) Bending moment.

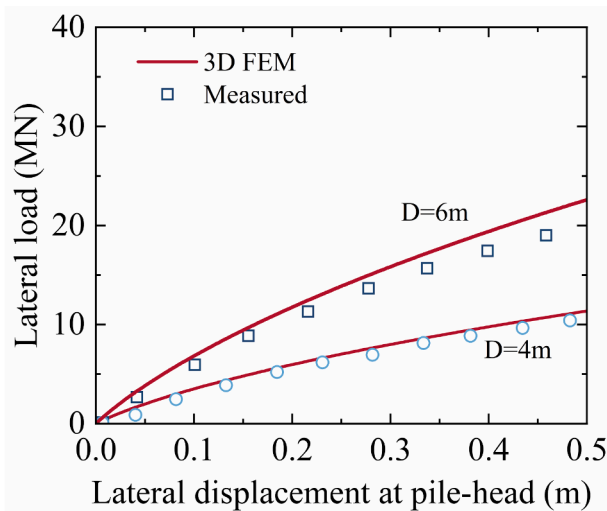


Fig. 8. Comparison of load–displacement response at pile head between centrifuge tests and numerical simulation.

Table 6
Program for the parametric analysis.

	Diameter D (m)	Load eccentricity (m)	Embedded length L (m)	L/D	Thickness t (m)
Kaolin clay	6	100	30	5	0.065
Bangkok	8			3.75	0.085
clay	10			3	0.105
Cowden	12			2.5	0.125
stiff clay	6		40	6.67	0.065
	8			5	0.085
	10			4	0.105
	12			3.33	0.125
	6		50	8.33	0.065
	8			6.25	0.085
	10			5	0.105
	12			4.17	0.125

applying Winkler foundation theory and finite element methods, the model can simulate the lateral displacement and bending moments along the pile shaft under various loading conditions.

4.4. Distributed lateral load soil reaction curve (p - y curve)

A systematic study on the effects of clay type, diameter, and embedment length on the p - y curves was conducted through parametric analysis. Figs. 12–14 presents the normalized p - y curves at two depths ($z = 0.2L$ and $0.9L$) for Kaolin clay, Bangkok clay, and Cowden stiff clay, respectively. It was observed that at the same depth, the normalized lateral soil resistance for monopiles of different diameters were basically consistent. For different clay foundations, the shape of the p - y curves are very similar, showing differences only in initial stiffness and the ultimate normalized lateral soil resistance. To standardize the representation of the p - y curves for different clay foundations, the hyperbolic function is introduced to represent the nonlinear characteristics of the normalized p - y curves.

Fig. 15 presents the distribution patterns of the ultimate resistance \bar{p}_u for monopiles with various length-to-diameter ratios in three types of clay foundations. From the figure, it is evident that \bar{p}_u in the wedge flow zone gradually increases with the increase of depth, reaching a peak in the full flow zone (the transition position between the wedge flow zone and the rotation deformation zone). It is also observed that the peak points are located around $0.5L$, which is in accordance with the conclusion of Cao et al. (2021). To achieve a unified expression of the maximum ultimate normalized distributed lateral load $\bar{p}_{u,max}$ among three different clay, by referring to the influencing factors of ultimate soil resistance in API and along with the results of Fig. 16, it was found that $\bar{p}_{u,max}$ among different clays is positively correlated with the ratio of effective vertical stress to undrained shear strength (σ'_v/s_u) at current depth. The final relationship is established as shown in Eq. (12). In Fig. 15, it can be seen that the rotation center is located near $0.75L$, where \bar{p}_u is close to zero. This is because large-diameter monopiles exhibit a deformation mode that rotates around the rotation center, so the lateral deformation at this center is always small throughout the deformation process, and thus the lateral soil resistance at this center cannot be fully mobilized. Since the shallow ultimate resistance is linearly distributed and the deep zone exhibits a symmetrical distribution pattern centered on the rotation center, a piecewise function is employed to characterize the influence of the rotational failure pattern

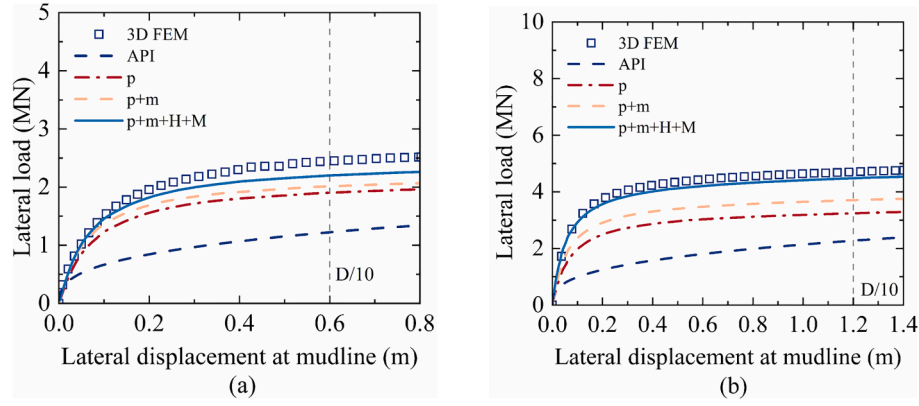


Fig. 9. Load-displacement curve with different soil reaction components at mudline (a) $L = 30$, $L/D = 5$ (b) $L = 30$, $L/D = 2.5$. Note that p represents the distributed lateral load, m represents the distributed moment, H signifies base shear force, and M stands for base moment.

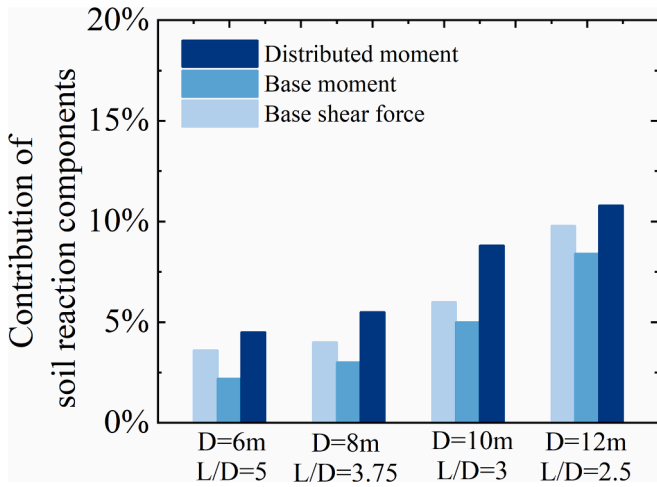


Fig. 10. Contribution of base moment, base shear force and distributed moment in Kaolin clay.

on the \bar{p}_u . The shallow zone is represented by a linear function, and the deep zone is represented by a hyperbolic tangent function. The distribution functions are shown in Eqs. (13)–(14), and the fitting is shown in Fig. 15.

The initial stiffness at each depth can be determined by fitting the hyperbolic function to the p - y curves (Cao et al., 2021). Fig. 17 presents the profile of the initial stiffness coefficient k_p of the normalized p - y curves with depth for the three different clay foundations. The parameter k_p increases with diameter along the depth, but the changes are not significant. Therefore, the effect of diameter on the parameter k_p is not considered in this paper (Byrne et al., 2020a). Given that the

parameter k_p gradually increases with depth and the variations are particularly significant near the rotation center, the exponential function of Eq. (15) is used to describe the overall distribution. Based on the results of the fitting, the relationship between parameters a_1 and b_1 and the average small strain shear modulus along the embedment length (G_{ave}) is established. Similar to the method of obtaining the ultimate resistance \bar{p}_u , and achieving a unified expression of the initial stiffness coefficient k_p of the normalized p - y curves on different clay foundations considering global distribution, the relationships between parameters a_1 and b_1 and G_{ave}/G_{ref} are established according to the results shown in Fig. 18, as presented in Eq. (16).

By following the proposed method, a unified p - y curve based on the hyperbolic function for monopiles in different types of clay foundations is finally established. Figs. 12–14 shows that the proposed curves can better represent the nonlinear characteristics of the soil reaction curves in different clay foundations.

Table 7

Normalized variables for the soil reaction components.

Normalized forms	Dimensionless formulas
Base moment, \bar{M}	$\frac{M_B}{s_u D^3}$
Base shear force, \bar{H}	$\frac{H_B}{s_u D^2}$
Pile side distributed moment, \bar{m}	$\frac{m}{ p D}$
Distributed lateral load, \bar{p}	$\frac{p}{s_u D}$
Pile cross-section rotation, $\bar{\theta}$	$\frac{\theta G_0}{s_u}$
Lateral displacement, \bar{y}	$\frac{y G_0}{s_u D}$

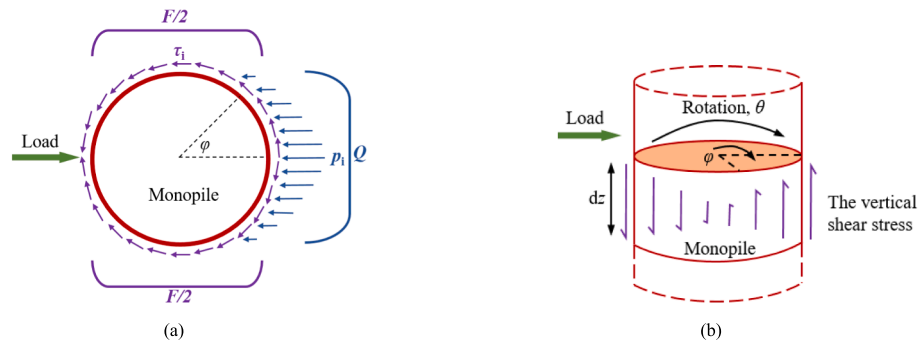


Fig. 11. Distribution of stress at the interface between the monopile and soil (a) normal soil stress and side shear stress (b) vertical shear stress.

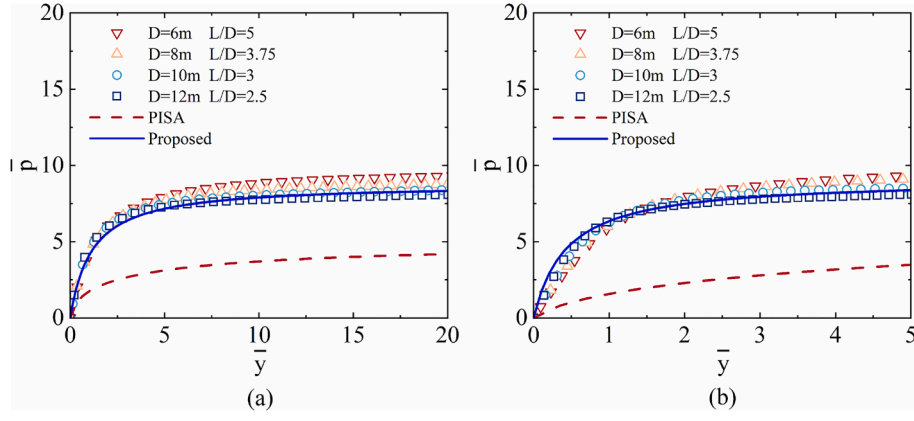


Fig. 12. Normalized p - y curve for Kaolin clay (PISA for $D = 10$ m) (a) $z = 6$ m (b) $z = 27$ m.

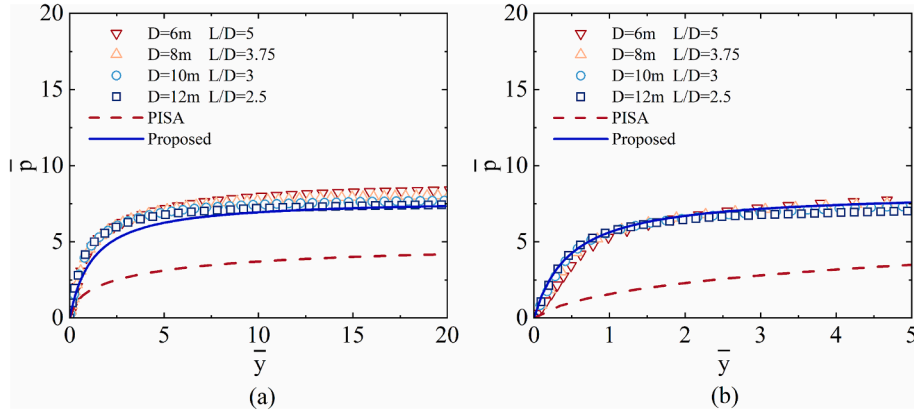


Fig. 13. Normalized p - y curve for Bangkok clay (PISA for $D = 10$ m) (a) $z = 6$ m (b) $z = 27$ m.

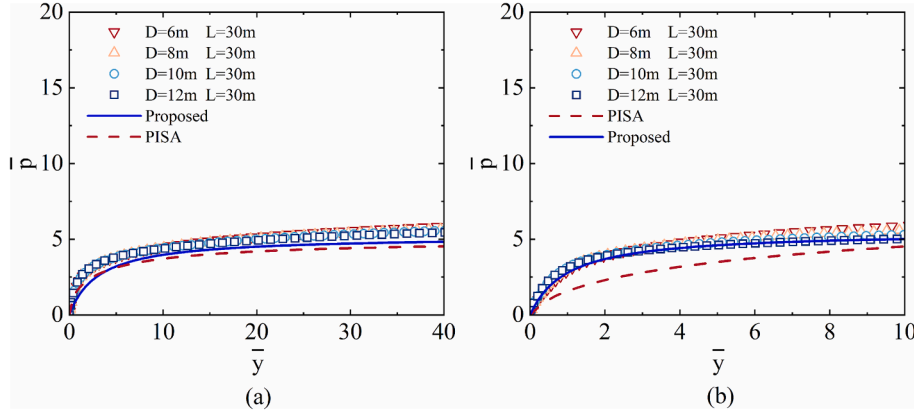


Fig. 14. Normalized p - y curve for Cowden Stiff clay (PISA for $D = 10$ m) (a) $z = 6$ m (b) $z = 27$ m.

$$\bar{p}_{u,\max} = 4.749 + 1.511 \frac{\sigma_v}{s_u} \quad (12)$$

$$\bar{p}_u = \bar{p}_{u,\max} (0.731 + 0.505 \frac{z}{L}) \quad z \leq 0.5L \quad (13)$$

$$\bar{p}_u = \bar{p}_{u,\max} \tanh(6.464 - 8.701z/L) \quad z > 0.5L \quad (14)$$

$$k_p = \alpha_1 e^{b_1 z/L} \quad (15)$$

$$k_p = 6.091 e^{(1.416 + 0.002 G_{ave}/G_{ref}) \cdot z/L - 0.01 G_{ave}/G_{ref}} \quad (16)$$

where, $\bar{p}_{u,\max}$ is the maximum ultimate lateral resistance, G_{ave} is the average small-strain shear modulus along the embedment length and G_{ref} is the reference modulus, equal to 1 MPa.

4.5. Distributed moment (m - θ curve)

The normalized distributed moment curves for Kaolin clay, Bangkok clay, and Cowden stiff clay are shown in Fig. 19. It initially decreases, then increases, and eventually stabilizes, which similar to the patterns of sand soil reaction curves (Burd et al., 2020; Zhang et al., 2024). Fig. 20 shows the distribution of the normalized ultimate distributed moment

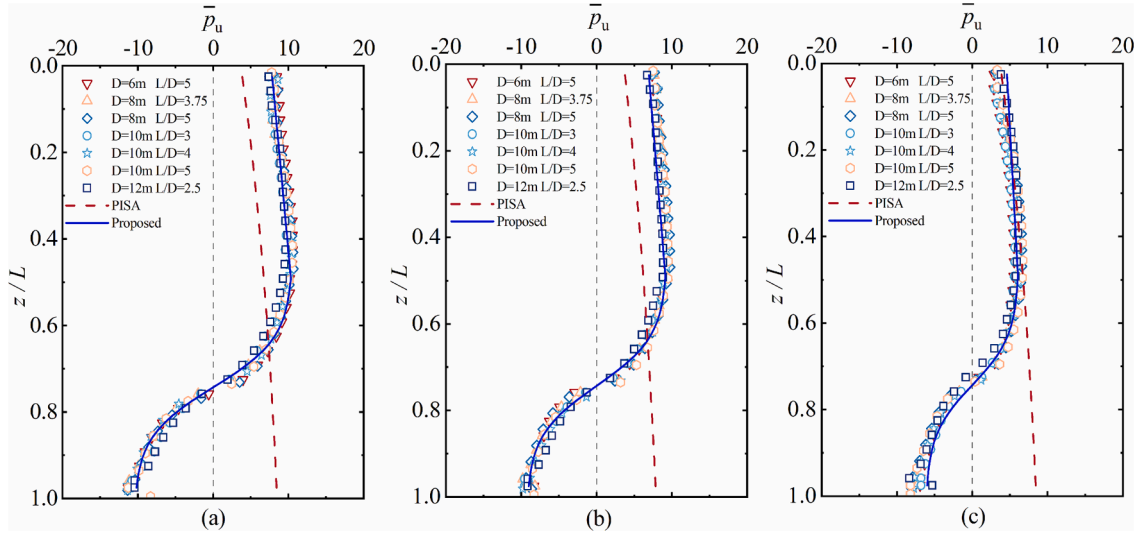


Fig. 15. Distribution of ultimate normalized distributed lateral load (PISA for $D = 10$ m) (a) Kaolin clay (b) Bangkok clay (c) Stiff clay.

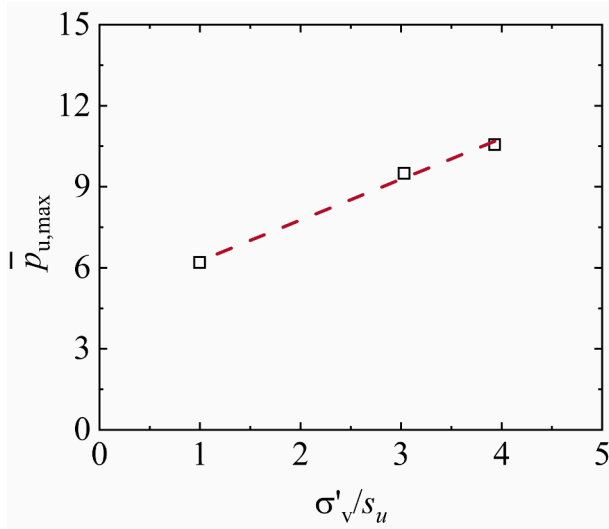


Fig. 16. Correlation between the maximum ultimate resistance and σ'_v/s_u at this depth among different clays.

(\bar{m}_u) with depth for three different clay foundations. It is observed that the effect of diameter on \bar{m}_u is minimal. The \bar{m}_u in different clays are basically at the same level and are not significantly affected by the type of clay or diameter, as the normalized distributed moment is related to the distributed soil resistance p . For simplicity and ease of use, a linear function in Eq. (17) is used to describe \bar{m}_u for the three different clays, with the fitting result illustrated in Fig. 20. According to the recommendations of Burd et al. (2020) and the characteristics of the normalized distributed moment soil reaction curves, the initial moment stiffness coefficient $k_m = 20$ is selected, and a unified distributed moment soil reaction curve is proposed, as shown in Fig. 19.

$$\bar{m}_u = 0.139 - 0.096 \frac{z}{L} \quad (17)$$

4.6. Base shear force and base moment

Fig. 21 shows the normalized base shear force curves for monopiles with different aspect ratios on three different clay foundations. It is evident that the normalized ultimate base shear force gradually decreases with the increase in diameter and varies between different clay foundations. By generalizing the relationship between the ultimate normalized base shear force, initial stiffness of monopiles, and clay characteristics, it is found that the ultimate normalized base shear force

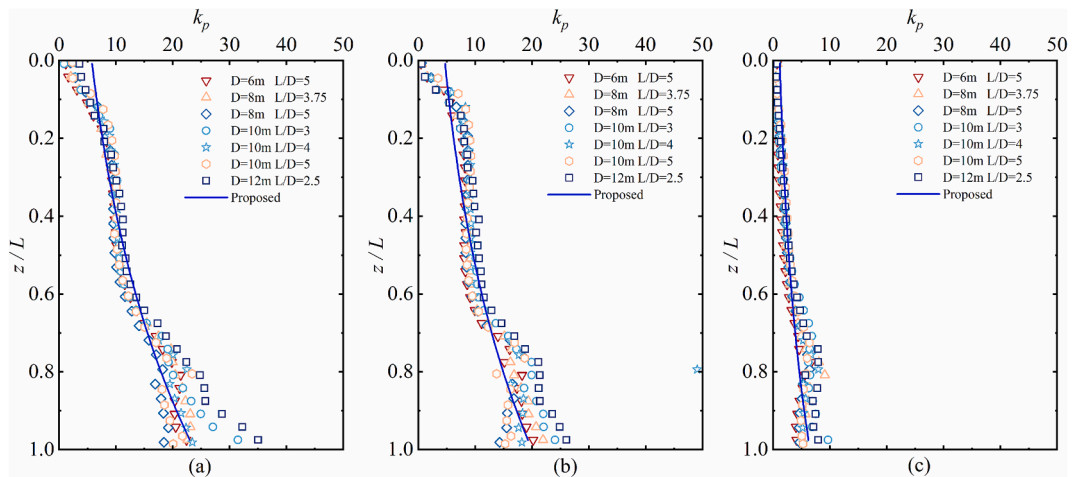


Fig. 17. Distribution of the initial stiffness coefficient (PISA for $D = 10$ m) (a) Kaolin clay (b) Bangkok clay (c) Stiff clay.

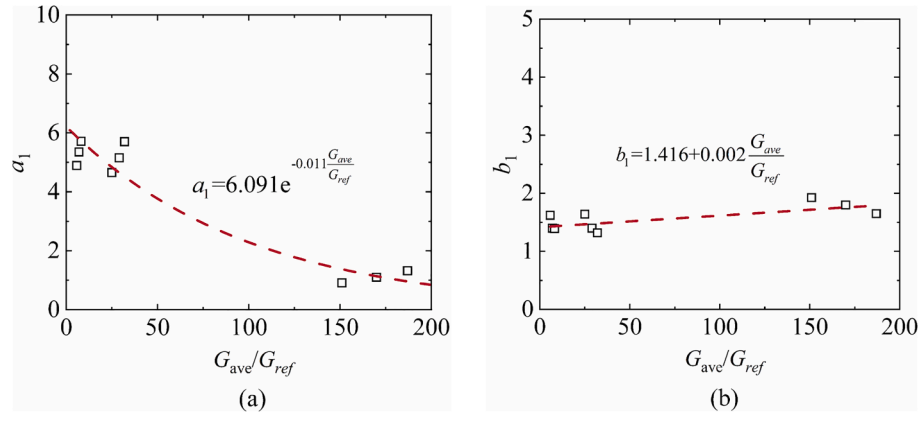


Fig. 18. Parameters related to the initial stiffness coefficient (a) a_1 (b) b_1 .

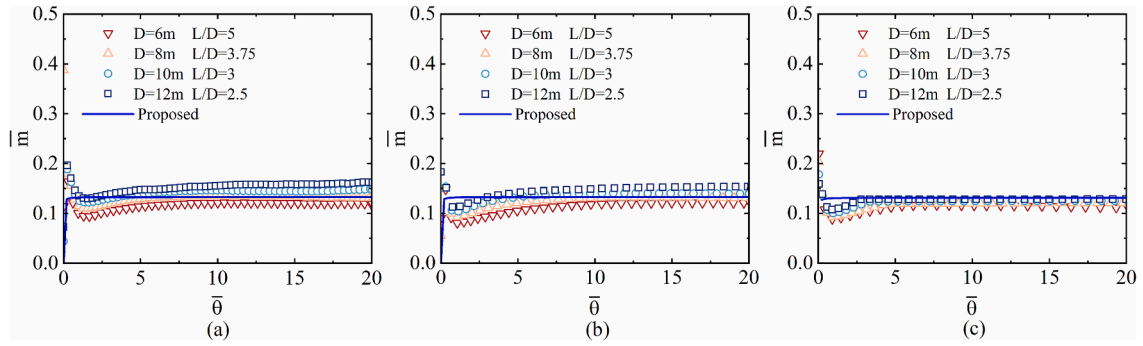


Fig. 19. Normalized $m-\theta$ curve ($z = 0.16L$) (a) Kaolin clay (b) Bangkok clay (c) Stiff clay.

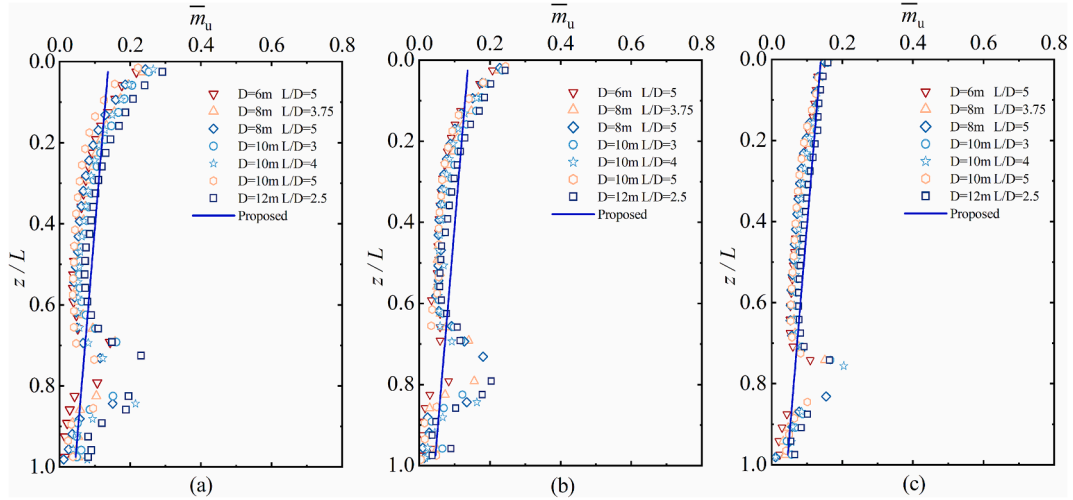


Fig. 20. Normalized ultimate distributed moment (a) Kaolin clay (b) Bangkok clay (c) Stiff clay.

of monopiles with the same diameter and embedded length on different clay foundations is positively correlated with σ'_v/s_u at pile base, and the initial shear stiffness coefficient is related to G_B/G_{ref} at this depth. Therefore, to simplify the considerations, the relationships are described using linear and exponential functions according to Eqs. (18)–(19) based on the calculation results. By summarizing and analyzing the relevant parameters a_2 , b_2 , c_2 , and d_2 , the relationships with the length-to-diameter ratio are finally established, as shown in Eqs. (20)–(21), and the result of the fitting is presented in Figs. 21–22.

Fig. 23 shows the normalized base moment soil reaction curves between the normalized base moment and pile cross-section rotation angle

for monopiles with different aspect ratios on three different clay foundations. It would appear that the normalized ultimate base moment increases as the diameter increases, but the change is relatively small. The normalized base moment soil reaction curves were studied using the same method with base shear force. According to Eqs. (22)–(23), the linear relationship between the normalized ultimate base moment and σ'_v/s_u at the same embedment length and diameter of monopiles on different clay foundations, and the relationship between the initial moment stiffness coefficient and G_B/G_{ref} were established. According to the aforementioned finding, the relationships between the parameters a_3 , b_3 , c_3 , and d_3 and length-to-diameter were also established using

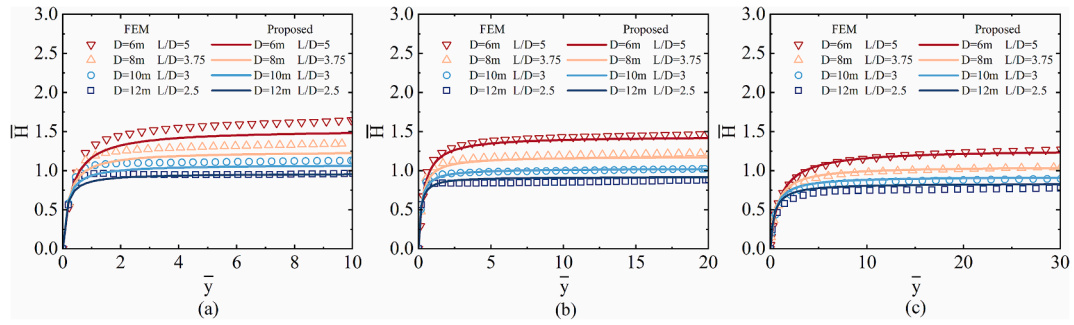


Fig. 21. Normalized base shear force soil reaction curves (a) Kaolin clay (b) Bangkok clay (c) Stiff clay.

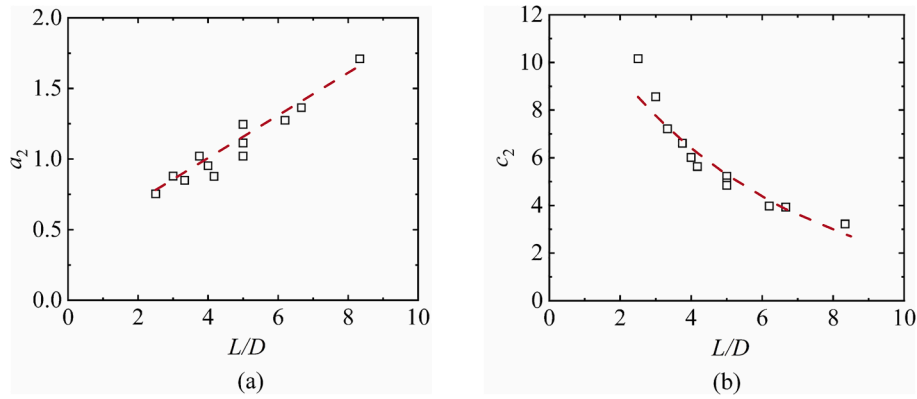


Fig. 22. Ultimate normalized base shear force soil reaction curves relevant coefficient (a) a_2 (b) c_2 .

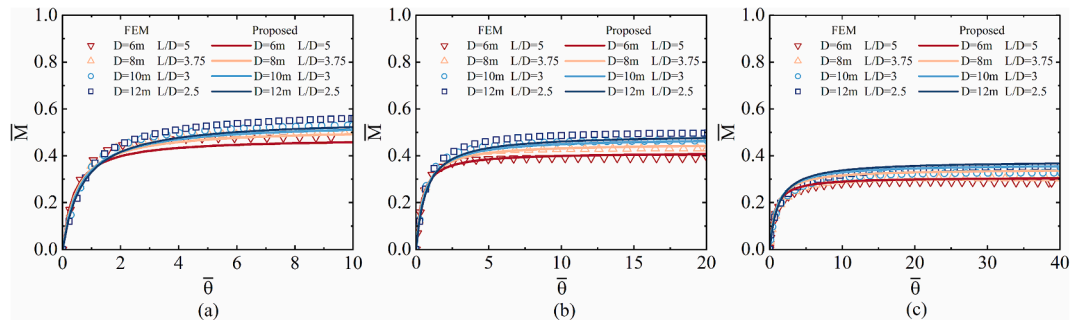


Fig. 23. Normalized base moment soil reaction curves (a) Kaolin clay (b) Bangkok clay (c) Stiff clay.

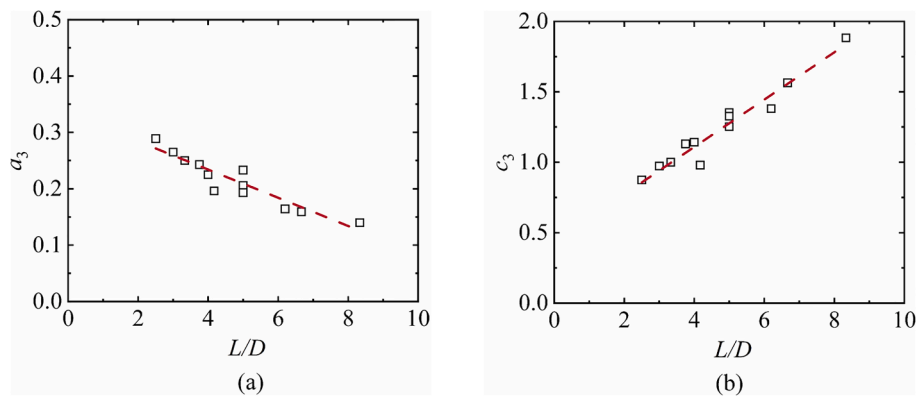


Fig. 24. Ultimate normalized base moment soil reaction curves relevant coefficient (a) a_3 (b) c_3 .

linear functions. The final results are shown in Eqs. (24) and (25), and the simulation result is shown in Fig. 23 and Fig. 24.

$$\bar{H}_{Bu} = a_2 + b_2 \frac{\sigma'_v}{s_u} \quad (18)$$

$$k_H = c_2 e^{d_2 \frac{G_B}{G_{ref}}} \quad (19)$$

$$\bar{H}_{Bu} = (0.404 + 0.151 \frac{L}{D}) + (0.019 \frac{L}{D}) \frac{\sigma'_v}{s_u} \quad (20)$$

$$k_H = 13.819 e^{-0.192 \frac{L}{D} - 0.007 \frac{G_B}{G_{ref}}} \quad (21)$$

$$\bar{M}_{Bu} = a_3 + b_3 \frac{\sigma'_v}{s_u} \quad (22)$$

$$k_M = c_3 e^{d_3 \frac{G_B}{G_{ref}}} \quad (23)$$

$$\bar{M}_{Bu} = (0.334 - 0.025 \frac{L}{D}) + (0.078 - 0.002 \frac{L}{D}) \frac{\sigma'_v}{s_u} \quad (24)$$

$$k_M = (0.437 + 0.168 \frac{L}{D}) e^{-0.005 G_B / G_{ref}} \quad (25)$$

where, G_B is the small-strain shear modulus at the pile base, G_{ref} is the reference modulus, equal to 1 MPa.

5. Verification of the unified model

To fully verify the unified soil reaction model proposed in this paper for predicting the laterally loaded response of monopiles in different types of clay foundations, the following three cases were selected for load–displacement curve comparison analysis. These are as follows: (1) 3D finite element validation of monopiles (3D FEM); (2) a field test on rigid piles conducted by Zdravković et al. (2019); (3) a centrifuge test on semi-rigid piles conducted by Lai et al. (2020). The soil parameters for the validation of the soil reaction model are given in Table 8 and the dimensions of the monopiles for which the validation was carried out are given in Table 9. G_0 and m_s are the small strain shear modulus coefficient and exponent, respectively, as expressed in the generalized plasticity constitutive model.

5.1. 3D finite element validation of monopiles

The monopile foundation of the DTU 10 MW wind turbine designed by Yang et al. (2020) was modeled according to the dimensions detailed in Table 9. Finite element simulations of laterally loaded monopiles were conducted on the three different clay foundations mentioned in the previous studies, using the constitutive parameters and soil reaction model parameters shown in Section 3.1. Fig. 25 compares the load–displacement curves obtained from the numerical analysis of monopiles in three different clay foundations with the predictions of the soil reaction model. It is apparent that the unified soil reaction model proposed in this study can effectively predict the laterally loaded capacity of large-diameter monopiles on various types of clay foundations

Table 8
Parameters of clay for verification.

Tests	Clay type	G_0	m_s	s_u (kPa)	γ' (kN/m ³)
3D FEM and Lai et al. (2020)	Kaolin clay	72	0.65	1.65z	6.5
3D FEM	Bangkok clay	260	0.5	3.3z	10
3D FEM and Byrne et al. (2020b)	Cowden stiff clay	1478	0.42	70 + 6.73z	11.37

Table 9
Monopile dimensions.

Tests	Embedded length (m)	Diameter (m)	Load eccentricity (m)	Thickness (m)
3D FEM	45	9	145	0.10
Byrne et al. (2020b)	10.5	2	10	0.025
Lai et al. (2020)	60	6	8	0.06

compared to the PISA model.

5.2. Verification of the rigid piles in Cowden stiff clay

Byrne et al. (2020b) conducted a series of laterally loaded field tests in stiff clay foundations at the Cowden site in the UK. This study selects the CL2 pile with a relatively large diameter for validation, with a monopile diameter (D) of 2 m, an embedment length (L) of 10.5 m, a loading height (e) of 10 m, and a thickness (t) of 0.025 m. On the basis of the research results of Byrne et al. (2020b), the undrained shear strength and small strain shear modulus of the stiff clay foundation can be obtained. Fig. 26 presents a comparison between the load–displacement curve observed at mudline in the field tests and the predictions of the proposed model. It is evident that the unified soil reaction model proposed can precisely predict the load–displacement curve of laterally loaded monopiles.

5.3. Verification of centrifuge tests on large diameter monopiles

Lai et al. (2020) carried out a centrifuge test on laterally loaded monopiles with a prototype pile diameter of 6 m in Kaolin clay. The prototype pile had a thickness of 0.06 m, an embedment length of 60 m, and a loading height of 8 m. The elastic modulus of the monopile was 210GPa. The effective unit weight of the clay is 6.5 kN/m³, and the undrained shear strength gradient is 1.65 kPa/m. Fig. 27 compares the predicted results of the proposed model with the load–displacement relationship measured from the centrifuge test. It can be apparent that the proposed model can reasonably predict the resistance of large-diameter laterally loaded monopiles.

6. Conclusions

Based on numerical analysis methods validated by centrifuge tests and field tests, a series of finite element analyses were conducted on lateral load monopiles in three different clay foundations. By establishing the relationship between stiffness coefficient and small strain shear modulus, and the relationship between ultimate soil resistance and the ratio of effective vertical stress and undrained shear strength, this paper proposes a unified soil reaction model suitable for soft and stiff clay foundations to accurately predict the lateral behavior of monopiles. The following conclusions can be drawn from the above analysis:

- (1) The maximum of the ultimate normalized distributed lateral load between different clays has a linear relationship with the ratio of effective vertical stress to undrained shear strength σ'_v/s_u at the current depth. The initial stiffness coefficient k_p varies significantly near the rotation center, and its distribution pattern is not influenced by the pile diameter. The initial stiffness coefficient k_p exhibits an exponential distribution, and a linear relationship can be established between the distribution parameters and the average small strain shear modulus across different types of clay.
- (2) The effect of diameter on the normalized ultimate distributed moment (\bar{m}_u) is minimal. The \bar{m}_u in different clays are basically at the same level and are not significantly affected by the type of clay or diameter.

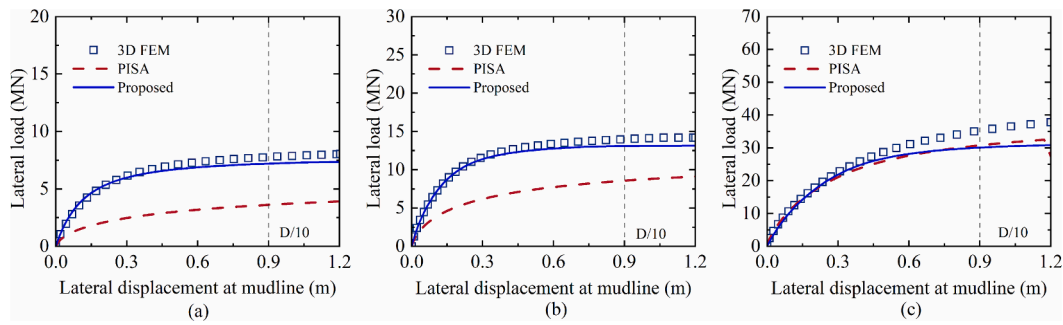


Fig. 25. Load-displacement relationship curve at mudline (a) Kaolin clay (b) Bangkok clay (c) Stiff clay.

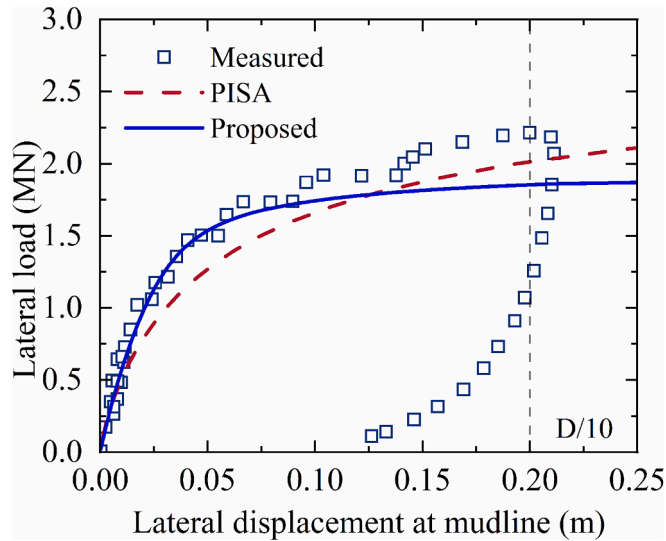


Fig. 26. Load-displacement relationship curve at mudline.

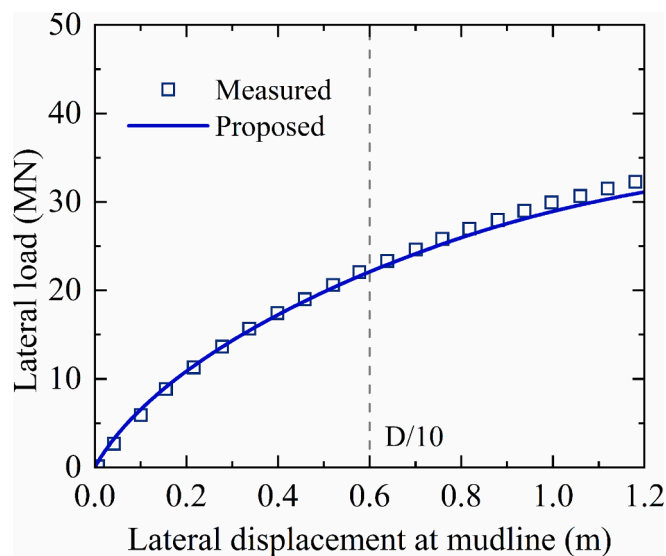


Fig. 27. Load-displacement relationship curve of large-diameter monopile at the pile head.

- (3) The normalized ultimate base moment and base shear force of monopiles with the same embedment length and diameter in different clay foundations can be represented by σ'_v/s_u at current depth. The initial shear stiffness coefficient and initial moment

stiffness coefficient can be represented by G_B/G_{ref} at this depth. Finally, the unified pile base moment and base shear force soil reaction curve can be established through the relationship between relevant parameters and the length-to-diameter ratio.

- (4) Through finite element analysis and validation with centrifuge and field tests, the proposed model in this paper is suitable for both soft and stiff clay. In addition, the applicability of the soil reaction model to layered soils under complex conditions can be studied in combination with the author's research in sand.

CRediT authorship contribution statement

Xiuyang Zhang: Writing – original draft, Validation, Software, Formal analysis. **Degao Zou:** Writing – review & editing, Supervision, Software, Funding acquisition. **Jingmao Liu:** Writing – review & editing, Supervision. **Kai Chen:** Software, Methodology. **Fanwei Ning:** Validation, Methodology. **Tianju Wang:** Validation, Formal analysis.

Declaration of competing interest

The authors declare that they have no known competing financial interests or personal relationships that could have appeared to influence the work reported in this paper.

Data availability

Data will be made available on request.

Acknowledgements

This research was funded by the National Natural Science Foundation of China (Grant Nos. 52109114, U2240211, and 52192674).

References

- API, 2014. Petroleum and natural gas industries-specific requirements for offshore structures. Part 4-geotechnical and foundation design considerations ISO 19901-4: 2003 (Modified). DC, Washington.
- Burd, H.J., Taborda, D.M.G., Zdravković, L., Abadie, C.N., Byrne, B.W., Houlsby, G.T., Gavin, K.G., Igoe, D.J.P., Jardine, R.J., Martin, C.M., McAdam, R.A., Pedro, A.M.G., Potts, D.M., 2020. PISA design model for monopiles for offshore wind turbines: application to a marine sand. *Geotechnique*. 70 (11). <https://doi.org/10.1680/jgeot.18.P.277>.
- Byrne, B.W., Houlsby, G.T., Burd, H.J., Gavin, K.G., Igoe, D.J., Jardine, R.J., Martin, C.M., McAdam, R.A., Potts, D.M., Taborda, D.M., 2020a. PISA design model for monopiles for offshore wind turbines: application to a stiff glacial clay till. *Geotechnique*. 70 (11), 1030–1047. <https://doi.org/10.1680/jgeot.18.P.255>.
- Byrne, B.W., McAdam, R.A., Burd, H.J., Beuckelaers, W.J., Gavin, K.G., Houlsby, G.T., Igoe, D.J., Jardine, R.J., Martin, C.M., Muir Wood, A., 2020b. Monotonic laterally loaded pile testing in a stiff glacial clay till at Cowden. *Geotechnique*. 70 (11), 970–985. <https://doi.org/10.1680/jgeot.18.PISA.003>.
- Cao, G., Ding, X., Yin, Z., Zhou, H., Zhou, P., 2021. A new soil reaction model for large-diameter monopiles in clay. *Comput. Geotech.* 137, 104311. <https://doi.org/10.1016/j.compgeo.2021.104311>.
- Chen, Z., Zhang, Z., Li, W., Wang, T., Zhang, J., 2023. Numerical study on the base shear force-displacement relationship for laterally loaded monopiles in dense sand. *Ocean Eng.* 286, 115527. <https://doi.org/10.1016/j.oceaneng.2023.115527>.

- Chen, K., Zou, D., Kong, X., 2017. A nonlinear approach for the three-dimensional polyhedron scaled boundary finite element method and its verification using Koyna gravity dam. *Soil Dyn. Earthq. Eng.* 96, 1–12. <https://doi.org/10.1016/j.soildyn.2017.01.028>.
- DNV, 2016. DNVGL-ST-0126: Support Structures for Wind Turbines, Oslo, Norway.
- Duque, J., Ochmański, M., Mašin, D., Hong, Y., Wang, L., 2021. On the behavior of monopiles subjected to multiple episodes of cyclic loading and reconsolidation in cohesive soils. *Comput. Geotech.* 134, 104049. <https://doi.org/10.1016/j.compgeo.2021.104049>.
- Duque, J., Roháč, J., Mašin, D., Najser, J., 2022. Experimental investigation on Malaysian kaolin under monotonic and cyclic loading: inspection of undrained Miner's rule and drained cyclic preloading. *Acta Geotech.* 17 (11), 4953–4975. <https://doi.org/10.1007/s11440-022-01643-0>.
- Fu, D., Zhang, Y., Aamodt, K.K., Yan, Y., 2020. A multi-spring model for monopile analysis in soft clays. *Mar. Struct.* 72, 102768. <https://doi.org/10.1016/j.marstruc.2020.102768>.
- Gong, J., Zou, D., Kong, X., Wang, D., Liu, J., Yu, X., 2023. A meshfree large-deformation analysis method for geotechnical engineering based on the RBF field variable mapping technology. *Comput. Method. Appl. M.* 416, 116377. <https://doi.org/10.1016/j.cma.2023.116377>.
- Goodman, R.E., Taylor, R.L., Brekke, T.L., 1968. A model for the mechanics of jointed rock. *J. Soil Mech. Found. Division.* 94 (3), 637–659. <https://doi.org/10.1061/JSEFAQ.0001133>.
- Hong, Y., He, B., Wang, L.Z., Wang, Z., Ng, C.W.W., Mašin, D., 2017. Cyclic lateral response and failure mechanisms of semi-rigid pile in soft clay: centrifuge tests and numerical modelling. *Can. Geotech. J.* 54 (6), 806–824. <https://doi.org/10.1139/cgj-2016-0356>.
- Jeanjean, P., 2009. Re-assessment of P-Y curves for soft clays from centrifuge testing and finite element modeling. *Offshore Technology Conference 20158*.
- Jiao, Y., Qiao, D., Wang, B., Tang, G., Lu, L., Ou, J., 2024. Three-spring soil reaction model for wind turbine monopile foundation in clay. *Appl. Ocean Res.* 144, 103911. <https://doi.org/10.1016/j.apor.2024.103911>.
- Lai, Y., Wang, L., Hong, Y., He, B., 2020. Centrifuge modeling of the cyclic lateral behavior of large-diameter monopiles in soft clay: Effects of episodic cycling and reconsolidation. *Ocean Eng.* 200, 107048. <https://doi.org/10.1016/j.oceaneng.2020.107048>.
- Lai, Y., Wang, L., Zhang, Y., Hong, Y., 2021. Site-specific soil reaction model for monopiles in soft clay based on laboratory element stress-strain curves. *Ocean Eng.* 220, 108437. <https://doi.org/10.1016/j.oceaneng.2020.108437>.
- Li, H., Tong, L., Liu, S., 2018. Effect of excavation unloading on p-y curves for laterally loaded piles. *Comput. Geotech.* 104, 131–139. <https://doi.org/10.1016/j.compgeo.2018.08.004>.
- Li, S., Yu, J., Huang, M., Leung, C.F., 2020. Application of T-EMSD based p-y curves in the three-dimensional analysis of laterally loaded pile in undrained clay. *Ocean Eng.* 206, 107256. <https://doi.org/10.1016/j.oceaneng.2020.107256>.
- Likitlersuang, S., Teachavorasinskun, S., Surarak, C., Oh, E., Balasubramaniam, A., 2013. Small strain stiffness and stiffness degradation curve of Bangkok Clays. *Soils Found.* 53 (4), 498–509. <https://doi.org/10.1016/j.sandf.2013.06.003>.
- Liu, P., Jiang, C., 2024. Analytical method for laterally loaded short piles near clay slopes considering the soil-pile-slope surface deformation mechanism. *Ocean Eng.* 296, 117036. <https://doi.org/10.1016/j.oceaneng.2024.117036>.
- Matlock, H., 1970. Correlations for design of laterally loaded piles in soft clay. *Proceedings of the Annual Offshore Technology Conference*, Houston, TX, United States.
- Naylor, D.J., 1974. Stresses in nearly incompressible materials by finite elements with application to the calculation of excess pore pressures. *Numerical Meth Eng.* 8 (3), 443–460. <https://doi.org/10.1002/nme.1620080302>.
- Pastor, M., Zienkiewicz, O.C., Leung, K.H., 1985. Simple model for transient soil loading in earthquake analysis. II. Non-associative models for sands. *Int. J. Numer. Anal. Met.* 9 (5), 477–498. <https://doi.org/10.1002/nag.1610090506>.
- Pastor, M., Zienkiewicz, O.C., Chan, A.H.C., 1990. Generalized plasticity and the modelling of soil behaviour. *Int. J. Numer. Anal. Met.* 14 (3), 151–190. <https://doi.org/10.1002/nag.1610140302>.
- Qu, Y., Zou, D., Kong, X., Yu, X., Chen, K., 2020. Seismic cracking evolution for anti-seepage face slabs in concrete faced rockfill dams based on cohesive zone model in explicit SBFEM-FEM frame. *Soil Dyn. Earthq. Eng.* 133, 106106. <https://doi.org/10.1016/j.soildyn.2020.106106>.
- Qu, Y., Zou, D., Chen, K., Liu, J., 2021. Three-dimensional refined analysis of seismic cracking and anti-seismic measures performance of concrete face slab in CFRDs. *Comput. Geotech.* 139, 104376. <https://doi.org/10.1016/j.compgeo.2021.104376>.
- Shao, X., Fu, Y., Jiang, C., 2024. Lateral soil-pile interaction of large-diameter rigid monopiles supporting OWTs in clay: Insights and an enhanced theoretical model. *Appl. Ocean Res.* 150, 104093. <https://doi.org/10.1016/j.apor.2024.104093>.
- Souri, A., Amirmojahedi, M., Abu-Farsakh, M., Voyiadis, G.Z., 2023. Development of unified p-y curve model for clays using finite element analysis of laterally loaded piles. *Can. Geotech. J.* 60 (7), 1055–1072. <https://doi.org/10.1139/cgj-2021-0014>.
- Surarak, C., Likitlersuang, S., Wanatowski, D., Balasubramaniam, A., Oh, E., Guan, H., 2012. Stiffness and strength parameters for hardening soil model of soft and stiff Bangkok clays. *Soils Found.* 52 (4), 682–697. <https://doi.org/10.1016/j.sandf.2012.07.009>.
- Truong, P., Lehan, B.M., 2018. Effects of pile shape and pile end condition on the lateral response of displacement piles in soft clay. *Geotechnique.* 68 (9), 794–804. <https://doi.org/10.1680/jgeot.16.P.291>.
- Wang, H., Fraser Bransby, M., Lehan, B.M., Wang, L., Hong, Y., 2022. Numerical investigation of the monotonic drained lateral behaviour of large-diameter rigid piles in medium-dense uniform sand. *Geotechnique.* 73 (8), 689–700. <https://doi.org/10.1680/jgeot.21.00149>.
- Wang, L., Lai, Y., Hong, Y., Mašin, D., 2020. A unified lateral soil reaction model for monopiles in soft clay considering various length-to-diameter (L/D) ratios. *Ocean Eng.* 212, 107492. <https://doi.org/10.1016/j.oceaneng.2020.107492>.
- Xu, B., Zou, D., Liu, H., 2012. Three-dimensional simulation of the construction process of the Zipingpu concrete face rockfill dam based on a generalized plasticity model. *Comput. Geotech.* 43, 143–154. <https://doi.org/10.1016/j.compgeo.2012.03.002>.
- Yang, Y., Bashir, M., Li, C., Michailides, C., Wang, J., 2020. Mitigation of coupled wind-wave-earthquake responses of a 10 MW fixed-bottom offshore wind turbine. *Renew. Energ.* 157, 1171–1184. <https://doi.org/10.1016/j.renene.2020.05.077>.
- Yu, J., Huang, M., Leung, C.F., Li, S., 2017a. Upper bound solution of a laterally loaded rigid monopile in normally consolidated clay. *Comput. Geotech.* 91, 131–145. <https://doi.org/10.1016/j.compgeo.2017.07.009>.
- Yu, J., Huang, M., Li, S., Leung, C.F., 2017b. Load-displacement and upper-bound solutions of a loaded laterally pile in clay based on a total-displacement-loading EMSD method. *Comput. Geotech.* 83, 64–76. <https://doi.org/10.1016/j.compgeo.2016.10.025>.
- Zdravković, L., Taborda, D.M.G., Potts, D.M., Abadías, D., Burd, H.J., Byrne, B.W., Gavin, K.G., Houlsby, G.T., Jardine, R.J., Martin, C.M., McAdam, R.A., Ushev, E., 2019. Finite-element modelling of laterally loaded piles in a stiff glacial clay till at Cowden. *Geotechnique.* 70 (11), 999–1013. <https://doi.org/10.1680/jgeot.18.PISA.005>.
- Zhang, Y., Andersen, K.H., 2017. Scaling of lateral pile p - y response in clay from laboratory stress-strain curves. *Mar. Struct.* 53, 124–135. <https://doi.org/10.1016/j.marstruc.2017.02.002>.
- Zhang, Y., Andersen, K.H., 2019. Soil reaction curves for monopiles in clay. *Mar. Struct.* 65, 94–113. <https://doi.org/10.1016/j.marstruc.2018.12.009>.
- Zhang, X., Zou, D., Liu, J., Chen, K., Li, X., Wang, T., 2024. A developed soil reaction model for large-diameter monopiles in sand based on hyperbolic curves. *Comput. Geotech.* 172, 106468. <https://doi.org/10.1016/j.compgeo.2024.106468>.
- Zhou, H., Liu, H., Ding, X., Kong, G., 2020. A p-y curve model for laterally loaded XCC pile in soft clay. *Acta Geotech.* 15 (11), 3229–3242. <https://doi.org/10.1007/s11440-020-00944-6>.
- Zhu, J., Yu, J., Huang, M., Shi, Z., Shen, K., 2022. Inclusion of small-strain stiffness in monotonic p-y curves for laterally loaded piles in clay. *Comput. Geotech.* 150, 104902. <https://doi.org/10.1016/j.compgeo.2022.104902>.
- Zou, D., Kong, X., Liu, J., Chen, K., Qu, Y., 2022a. Theoretical Introduction and User Manual of the GEODYNA 7.0: a High-Performance Finite Element Analysis Software System for Large-Scale Geotechnical Engineering. Dalian: Institute of earthquake engineering, Dalian University of Technology, Dalian.
- Zou, D., Jiang, Q., Liu, J., Jin, W., Zhu, X., 2022b. Characteristics and mechanism of inhomogeneous pore pressure of core wall in super-high rockfill dam. *Shuili Xuebao.* 53 (12), 1467–1475 (in chinese).
- Zou, D., Xu, B., Kong, X., Liu, H., Zhou, Y., 2013. Numerical simulation of the seismic response of the Zipingpu concrete face rockfill dam during the Wenchuan earthquake based on a generalized plasticity model. *Comput. Geotech.* 49, 111–122. <https://doi.org/10.1016/j.compgeo.2012.10.010>.